PAPER

Check for updates

Strongly enhanced luminescence of Sr₄Al₁₄O₂₅:Mn⁴⁺ phosphor by co-doping B³⁺ and Na⁺ ions with red emission for plant growth LEDs

Strongly enhanced luminescence of $Sr_4Al_{14}O_{25}$:Mn^{4+} phosphor by co-doping B^{3+} and Na^+ ions with red emission for plant growth LEDs

Jiaqi Long, Xuanyi Yuan, Chaoyang Ma, Miaomiao Du, Xiaoli Ma, Zicheng Wen, Ran Ma, Yuzhen Wang and Yongge Cao [ID] *

Development of a more cost-effective radiation source for use in plant-growing facilities would be of significant benefit for commercial crop production applications. A series of co-doped B^{3+} and Na^+ ions $Sr_4Al_{14}O_{25}$:Mn^{4+} inorganic luminescence materials which can be used for plant growth were successfully synthesized through a conventional high-temperature solid-state reaction. Powder X-ray diffraction was used to confirm the crystal structure and phase purity of the obtained samples. Then scanning electron microscopy elemental mapping was undertaken to characterize the distribution of the doped ions. Detail investigations on the photoluminescence emission and excitation spectra revealed that emission intensity of tetravalent manganese ions can be well enhanced by monovalent sodium ions and trivalent boron ions under near-ultraviolet and blue excitation. Additionally, crystal field parameters and energies of states are calculated and discussed in detail. Particularly we achieve a photoluminescence internal quantum yield as high as 60.8% under 450 nm blue light excitation for $Sr_4Al_{14}O_{25}$:Mn^{4+}, Na^+, B^{3+}. Therefore, satisfactory luminescence properties make these phosphors available to LEDs for plant growth.

Introduction

It is known that green plants can be grown only using red and blue monochromatic light, because chlorophyll has its second distinct absorption peak in the vicinity of 450 nm (the blue light region) and its first peak in the vicinity of 660 nm (red light region). The blue light is indispensable to the morphologically healthy plant growth, and the red light contributes to the plant leaf photosynthesis.[1,2] The first successful plant growth experiment using only blue and red LEDs were achieved in June 1994 by Okamoto and Yanagi.[3]

With LEDs price reduced, LEDs are gradually used as plant lighting source, because of its high light efficiency, energy saving and other characteristics. As the driving currents of the blue chip and the red chip are inconsistent, the design of the driver circuit of LEDs for planet growth would be very complex, resulting in increased cost. Therefore, the plant-grown red lamp that is currently in widespread use in the marketplace is composed of a red phosphor rather than a red chip. The most commonly used red phosphors are nitride phosphor (*e.g.*, $Sr_2Si_5N_8$:Eu^{2+}, $CaAlSiN_3$:Eu^{2+}) because of high luminous efficiency. But their high temperature (~1600 °C), high pressure (1–10 MPa) preparation conditions and expensive raw materials containing rare earth elements lead to high cost.[4]

In recent years, Mn^{4+}-activated fluoride compounds, as an alternative to commercial (oxy)nitride phosphors, are emerging as a new class of non-rare-earth red phosphors for high-efficacy warm white LEDs[5] compared to Mn^{4+}-activated fluoride phosphor, the emission wavelength of Mn^{4+}-activated oxide phosphors, such as $Sr_4Al_{14}O_{25}$:Mn^{4+}, $Y_3Al_5O_{12}$:Mn^{4+}, *etc.*, is much longer which is very suitable for plant lighting, because the absorption peak of plant chlorophyll is near 660 nm. The following diagram shows spectroscopic range of Mn^{4+} ions in various crystals.[6] We can see from Fig. 1 that the emission peak of the Mn^{4+}-activated fluoride phosphor and the absorption peak of chlorophyll rarely overlap, while the emission peak of the Mn^{4+}-activated oxide phosphors, such as $Sr_4Al_{14}O_{25}$:Mn^{4+}, overlap with the absorption peaks of chlorophyll-a and chlorophyll-b.

As shown in Fig. 2, the emission spectrum of $Sr_4Al_{14}O_{25}$:Mn^{4+} red phosphor has overlap more efficiently with the absorption spectrum of chlorophyll compared with $Sr_2Si_5N_8$:Eu^{2+} red commercial phosphors. However, most Mn^{4+}-activated oxide phosphors cannot be excited effectively by blue light, which limited its application on blue chip-based LEDs. There are some methods to improve the luminous efficiency and luminous intensity of Mn^{4+}-activated oxide phosphors, such as impurity doping with Mg^{2+} ions,[8,9] impurity doping with Bi^{3+} ions, and impurity doping with Na^+ ions.[10–12] The objective of this work is to develop a red emitting phosphor which can match with blue chip for possible application in plant growth. In this article, the red phosphors $Sr_4Al_{14}O_{25}$:Mn^{4+}, Na^+, B^{3+} with strong absorption at blue region were synthesized. The difference with

Beijing Key Laboratory of Opto-electronic Functional Materials & Micro-nano Devices, Department of Physics, Renmin University of China, Beijing 100872, China. E-mail: caoyongge@ruc.edu.cn
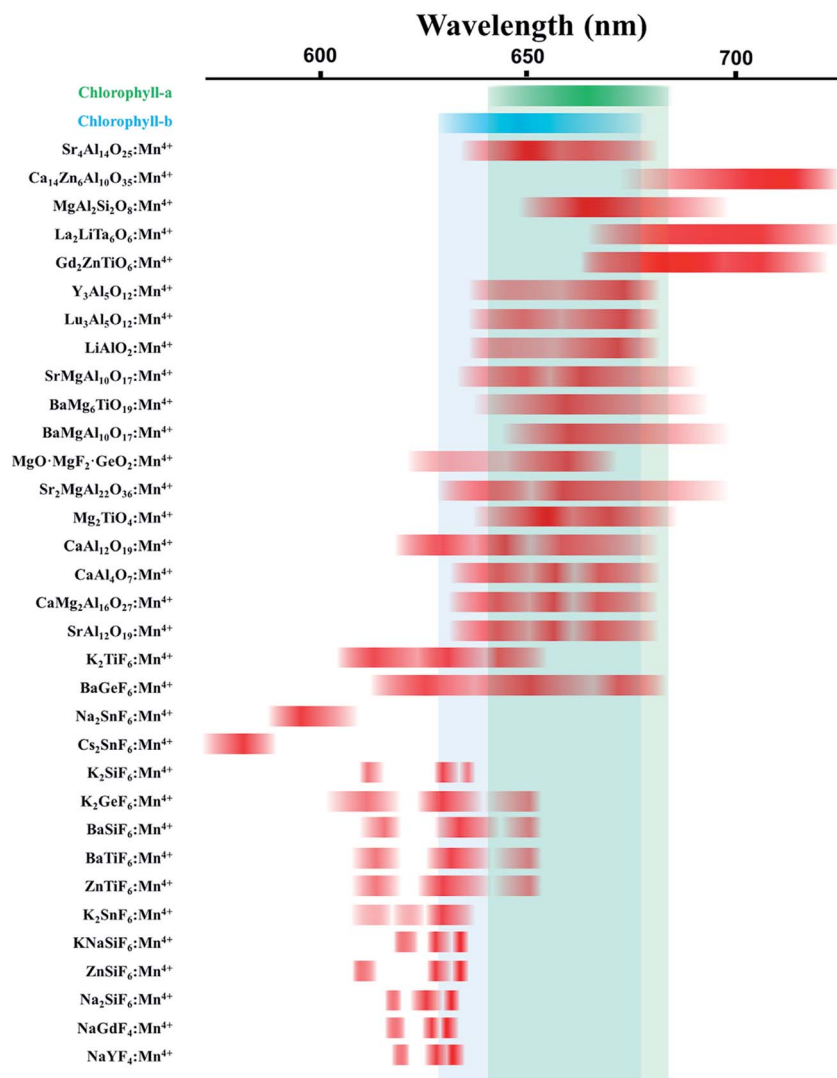
Fig. 1 Spectroscopic range of Mn^{4+} ions in various crystals. Green and blue color indicate the absorption spectrum region of chlorophyll–a and chlorophyll–b, respectively. Red color indicates the emission spectrum region of various phosphors with Mn^{4+} ions doped.

$Sr_4Al_{14}O_{25}$:Mn^{4+}, Na^+ phosphors reported by Lili Meng[12] was that the excitation intensity of the phosphor we prepared was significantly improved, especially in the blue light region. We also found that the doping amount of B^{3+} ions was very crucial. Specific doping ratio of B^{3+} ions and Na^+ ions make the luminous performance of the phosphor significantly improved. The advancements of current work include significant improvement of luminescent efficiency of $Sr_4Al_{14}O_{25}$:Mn^{4+} by doping B^{3+} and Na^+ ions. Notably, doping of B^{3+} and Na^+ ions can improve its visible light excitation efficiency in the spectral range of 400–500 nm so that it can be incorporated as a red component into blue chip-based LED applications for plant growth.

Experimental section

Materials and synthesis

Polycrystalline phosphors with composition of $Sr_4Al_{14}O_{25}$:Mn^{4+}, Na^+, B^{3+} were prepared with a high-temperature solid-state reaction. Briefly, the constituent raw materials $SrCO_3$ (A. R., 99.9%), Al_2O_3 (A. R., 99.99%), Na_2CO_3 (A. R., 99%), H_3BO_3 (A. R., 99%) and MnO_2 (A. R., 99.99%) were weighed according to the stoichiometric ratio. Individual batches of 10 g were weighted according to the designed stoichiometry and mixed homogeneously with the same mass of absolute ethyl alcohol as the dispersant. After planetary ball-milling process, the obtained homogeneous slurry was placed in a Petri dish and dried in an oven. Then, the dried mixtures were put into a crucible with a lid and heated in a tubular furnace at 1400 °C for 6 hours in the air. When cooled down to room temperature, the prepared phosphors were crushed and ground for subsequent measurements.

Characterization

All crystal structure compositions were checked for phase formation by using powder X-ray diffraction (XRD) analysis with a Rigaku X-ray diffractometer (Tokyo, Japan) with a graphite
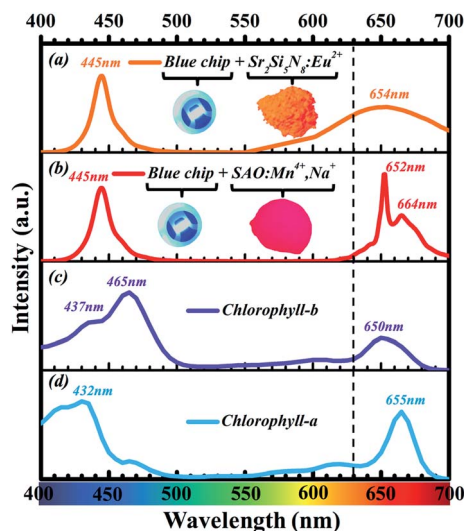
Fig. 2   (a) Emission spectrum of LEDs fabricated with 445 nm blue chip and $Sr_2Si_5N_8:Eu^{2+}$ red phosphor. (b) Emission spectrum of LEDs fabricated with 445 nm blue chip and $Sr_4Al_{14}O_{25}:Mn^{4+}$, red phosphor. (c) Absorption spectrum of chlorophyll-b. (d) Absorption spectrum of chlorophyll-a (redrawn from Zscheile and Comar's (1941) original data[7]).

monochromator using Cu Kα radiation ($\lambda = 1.54056$ Å), over the angular range $10° < 2\theta < 80°$, operating at 40 kV and 40 mA. The schematic crystal structure of $Sr_4Al_{14}O_{25}$ was drawn in VESTA.[13] The photoluminescence (PL) and photoluminescence excitation (PLE) spectra of the samples were analyzed by using a Hitachi F-7000 spectrophotometer (Tokyo, Japan) with a 150 W Xe lamp.

Results and discussion

Microstructure

The compositions of the typical $Sr_4Al_{14}O_{25}:0.014Mn^{4+}$, xB^{3+}, $0Na^+$, $(0 \leq x \leq 1.6)$ samples were displayed in Fig. 3a. When no flux is added, the compound $Sr_4Al_{14}O_{25}$ is not formed, and instead, the two phases $SrAl_2O_4$ (JCPDS-No. 34-0379) and $SrAl_{12}O_{19}$ (JCPDS-No. 80-1195) appear. When boric acid is added, for instance at $x = 0.2$, the sample turns into a single phase of $Sr_4Al_{14}O_{25}$. With increase of x from 0.2 to 1.2, XRD patterns of phosphors agree well with that of standard $Sr_4Al_{14}O_{25}$ (JCPDS-No. 52-1876). Further increment of boric acid content will induce an extra impurity phase of $SrAl_2O_4$. Because boric acid has lower melting temperature, it (after being homogeneously dispersed throughout the sample) will be the first component in the mixture to melt at high temperature. This can promote the immigration of Sr and Al ions, for instance by diffusion, and increase the possibility that the ions encounter, and thus accelerate the crystallization process. Excess boron will dilute the content of Sr and Al ions in the sample and it is therefore not beneficial for the formation of the phase $Sr_4Al_{14}O_{25}$. According to the emission spectrum (Fig. 7b), it is concluded that the optimum x of B^{3+} is 0.8. Comparison of B^{3+} dopant content in $Sr_4Al_{14}O_{25}:Mn^{4+}$, xB^{3+} is shown in Table 1. The compositions of the typical $Sr_4Al_{14}O_{25}:0.014Mn^{4+}$, $0.8B^{3+}$,
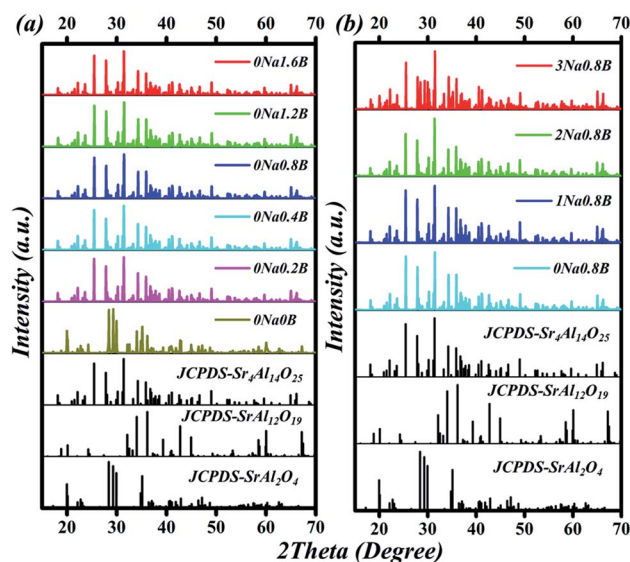
Fig. 3   (a) XRD patterns of $Sr_4Al_{14}O_{25}:0.014Mn^{4+}$, xB^{3+}, $0Na^+$ ($0 \leq x \leq$ 1.6) phosphors. (b) XRD patterns of $Sr_4Al_{14}O_{25}:0.014Mn^{4+}$, $0.8B^{3+}$, yNa^+ ($0 \leq y \leq 3$). The reference spectra of $Sr_4Al_{14}O_{25}$ (JCPDS-No. 52-1876), $SrAl_{12}O_{19}$ (JCPDS-No. 80-1195), $SrAl_2O_4$ (JCPDS-No. 34-0379) standard patterns were shown at the bottom.

Table 1   Comparison of B^{3+} dopant content in $Sr_4Al_{14}O_{25}:Mn^{4+}$, xB^{3+}

Range of x	Optimum value of x	Ref.
—	0.4	12
—	0.54	14
0–3.5	0.7	15
0–1.6	0.8	This work

yNa^+, $(0 \leq y \leq 3)$ samples were displayed in Fig. 3b. With increase of y from 0 to 2, XRD patterns of phosphors agree well with that of standard $Sr_4Al_{14}O_{25}$ (JCPDS-No. 52-1876). Further increment of Na^+ content will induce an extra impurity phase of $SrAl_2O_4$.

Fig. 4 shows a schematic of the $Sr_4Al_{14}O_{25}$ crystal structure. The space group of $Sr_4Al_{14}O_{25}$ is *Pmma* and orthorhombic. The networks of orthorhombic $Sr_4Al_{14}O_{25}$ are built by one layer of the octahedral anion groups (AlO_6) and several layers of tetrahedral anion groups (AlO_4) alternatively. There are three types of AlO_6 octahedrons ($Al(4)O_6$, $Al(5)O_6$ and $Al(6)O_6$) and three types of AlO_4 tetrahedron ($Al(1)O_6$, $Al(2)O_6$ and $Al(3)O_6$). Compared with the strong covalence effect of the AlO_4 tetrahedron, a little weak polarization field of the AlO_6 octahedron is more suitable for Mn^{4+} incorporating. In addition, the Mn^{4+} ion always experiences a strong CF due to its high effective positive charge with the result that the emission spectrum is always dominated by the sharp emission line corresponding with the spin-forbidden $^2E_g \rightarrow {}^4A_{2g}$ transition.[16]

Luminescence property

Fig. 5a show the PLE spectrum of $Sr_4Al_{14}O_{25}:0.8B^{3+}$, $2Na^+$, zMn^{4+} ($0.05\% \leq z \leq 0.5\%$) phosphor monitored at 652 nm. Fig. 5b show the PL spectrum of $Sr_4Al_{14}O_{25}:0.8B^{3+}$, $2Na^+$, zMn^{4+} (0.05%
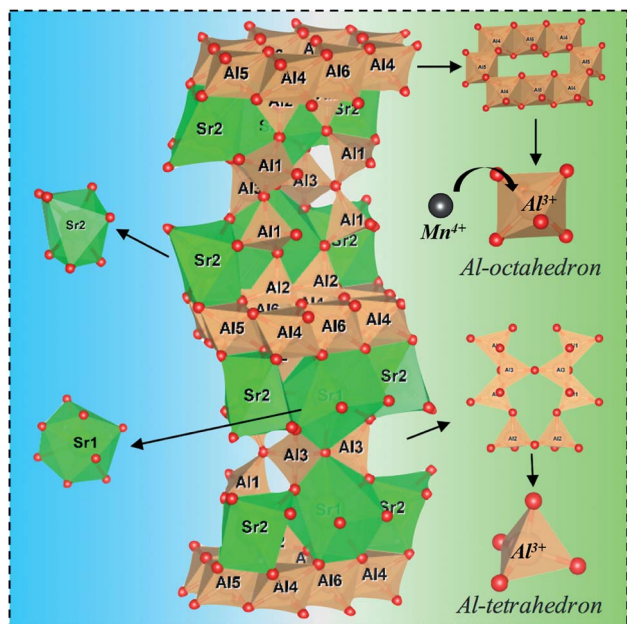
Fig. 4 Schematic illustration of crystal structure of $Sr_4Al_{14}O_{25}$. Black ball: Mn; Green ball: Sr; red ball: O; and brown ball: Al. Brown polyhedron: AlO_6-octahedron/AlO_4-tetrahedron; green polyhedron: SrO_7/SrO_8.

$\leq z \leq 0.5\%$) phosphor excited at 450 nm. Fig. 5c and d visually show the excitation and emission intensity of Mn^{4+} on dopant concentration for $Sr_4Al_{14}O_{25}:0.8B^{3+}$, $2Na^+$, zMn^{4+} phosphor, respectively. As we can see, the optimum molar concentration of Mn^{4+} in $Sr_4Al_{14}O_{25}:0.8B^{3+}$, $2Na^+$, zMn^{4+} in this work was 0.1 mol%. The photoluminescence emission spectrum of the phosphor presented a double-peak structure between 600 and 700 nm with two strong bands at about 654 and 664 nm, which were attributed to the $^2E \rightarrow {}^4A_2$ transition of Mn^{4+} ions and a phonon sideband transition, respectively.[13]

After obtained optimum Mn^{4+} doping concentration, we adjusted the amount of B^{3+} and Na^+. Fig. 6a and b show the photographs of $Sr_4Al_{14}O_{25}:0.014Mn^{4+}$, xB^{3+}, yNa^+ ($0 \leq x \leq 1.6$, $0 \leq y \leq 3$) under natural sunlight and 365 nm UV light, respectively. Along with Na^+ ions and B^{3+} doping concentrations increasing, the color of $Sr_4Al_{14}O_{25}:0.014Mn^{4+}$, xB^{3+}, yNa^+ phosphors under natural sunlight change from light yellow to bright yellow. This might be ascribed to the Na^+ and B^{3+} ions enhanced absorption band (220–500 nm), especially in the region of 400–500 nm, as illustrated in Fig. 7a.

In detail, Fig. 7a shows PLE spectrum of $Sr_4Al_{14}O_{25}:0.014Mn^{4+}$, xB^{3+}, yNa^+ phosphor monitored at 652 nm. In order to compare the relative changes of the excitation bands, the PLE intensity is normalized. When no Na^+ is added, with x of B^{3+}
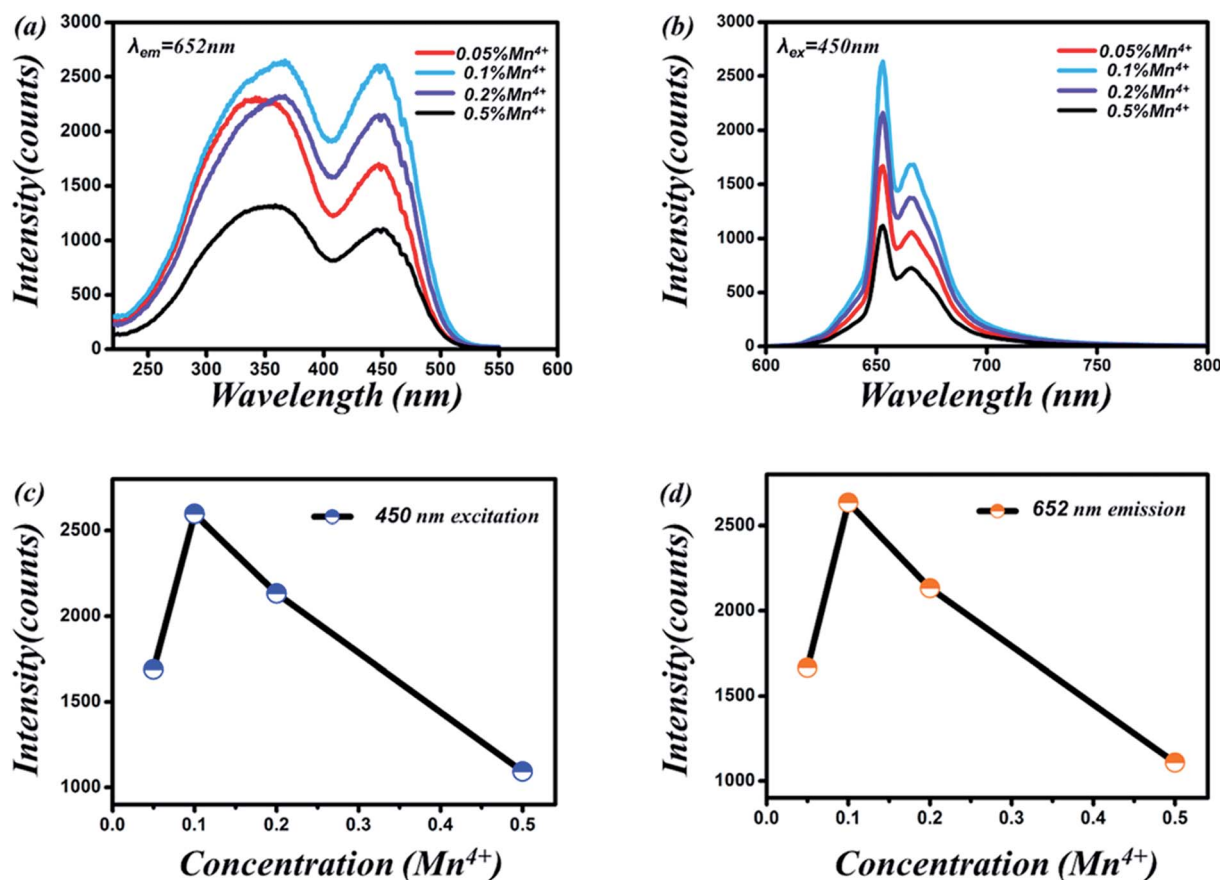

Fig. 5 (a) PLE spectrum of $Sr_4Al_{14}O_{25}:0.8B^{3+}$, $2Na^+$, zMn^{4+} ($0.05\% \leq z \leq 0.5\%$) phosphor monitored at 652 nm. (b) PL spectrum of $Sr_4Al_{14}O_{25}:0.8B^{3+}$, $2Na^+$, zMn^{4+} phosphor excited by 450 nm blue light. (c) Dependence of Mn^{4+} PLE intensity on dopant concentration for $Sr_4Al_{14}O_{25}:0.8B^{3+}$, $2Na^+$, zMn^{4+} phosphor. (d) Dependence of Mn^{4+} PL intensity on dopant concentration for $Sr_4Al_{14}O_{25}:0.8B^{3+}$, $2Na^+$, zMn^{4+} phosphor.
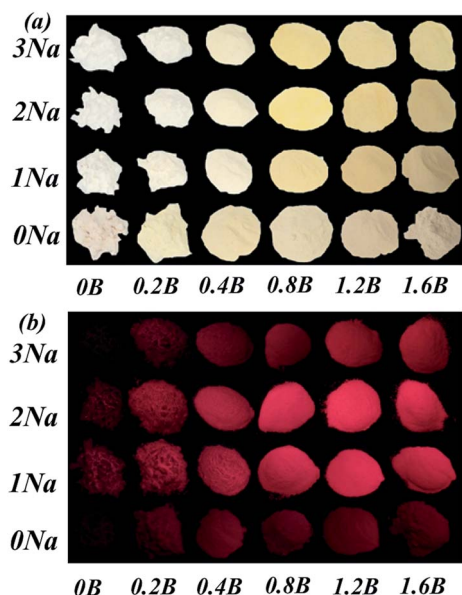
Fig. 6 (a) Photographs of Sr$_4$Al$_{14}$O$_{25}$:0.014Mn^{4+}, xB^{3+}, yNa$^+$ (0 ≤ x ≤ 1.6, 0 ≤ y ≤ 3) under natural sunlight. (b) Photographs of Sr$_4$Al$_{14}$O$_{25}$:0.014Mn^{4+}, xB^{3+}, yNa$^+$ under 365 nm UV light.
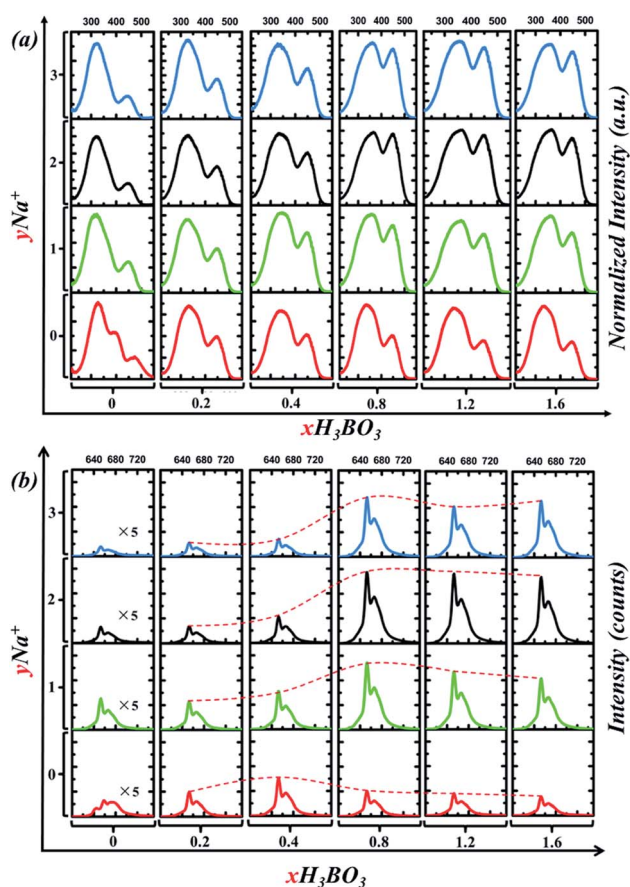
Fig. 7 (a) PLE spectrum of Sr$_4$Al$_{14}$O$_{25}$:0.014Mn^{4+}, xB^{3+}, yNa$^+$ phosphor monitored at 652 nm. (b) PL spectrum of Sr$_4$Al$_{14}$O$_{25}$:0.014Mn^{4+}, xB^{3+}, yNa$^+$ phosphor excited by 450 nm blue light.

increases from 0.2 to 1.6, the relative magnitude of excitation bands varies little. Furthermore, the optimum x of B^{3+} is 0.4, not 0.8, according to Fig. 7b. When Na$^+$ is added, for instance at $y = 1$, the intensity of the blue excitation band (400–500 nm) has been dramatically increased, as shown in Fig. 7a. In Fig. 7b, we can see that the optimum x of B^{3+} turns to 0.8 from 0.4. When x of B^{3+} is fixed at 0.8, the emission intensity increased first, reached the maximum ($y = 2$), and then decreased with the increase of Na$^+$ content. Cross experiment can clearly found that the optimal combination is $x = 0.8$, $y = 2$. To illustrate the difference between our experimental results and Meng's,[12] the detail differences are listed in Table 2. As we can see the amount of doping Na$^+$ and B^{3+} is observably different. As Fig. 7a shown, when $x = 0.4$, the addition of Na$^+$ does not significantly affect the relative intensity between the two excitation bands. This is why Meng didn't report the asynchronous increase of excitation bands. This asynchronous increase of excitation bands, however, allows the phosphor to be more easily excited by blue light. As Fig. 7b shows, the PL emission intensity excited by 450 nm blue light sharply increased 3 times when x of B^{3+} turns to 0.8 from 0.4 (when $y = 2$). Therefore, addition of B^{3+} and Na$^+$ ions in Sr$_4$Al$_{14}$O$_{25}$:0.014Mn^{4+}, xB^{3+}, yNa$^+$ can significantly improve its visible light excitation efficiency in the spectral range of 400–500 nm so that it can be incorporated as a red component into blue chip-based LED applications for plant growth.

Fig. 8a and b show the photoluminescent excitation and emission spectra of the Sr$_4$Al$_{14}$O$_{25}$:0.014Mn^{4+}, 0.8B^{3+} based phosphors with or without co-incorporating Na$^+$. The fluorescent intensities of the phosphors excited at 450 nm reached a maximum at $x = 0.8$, $y = 2$ and $z = 0.014$, and the strongest emission intensity of Sr$_4$Al$_{14}$O$_{25}$:0.8B^{3+}, 2Na$^+$, 0.014Mn^{4+} sample were increased by 700% compared with Sr$_4$Al$_{14}$O$_{25}$:0.8B^{3+}, 0.014Mn^{4+} without Na$^+$ co-doping. The photographs of the Sr$_4$Al$_{14}$O$_{25}$:0.014Mn^{4+}, 0.8B^{3+}, 2Na$^+$ sample and Sr$_4$Al$_{14}$O$_{25}$:0.014Mn^{4+}, 0.8B^{3+} sample exposed to 450 nm blue light and 365 nm UV light are shown in the insert of the Fig. 8a and b. After the incorporating of sodium ions, the brightness of phosphor becomes larger. We can find that the excitation spectra are consists of three conjoint bands by multi-peaks fitting, which located from near UV region to visible blue region. These three bands are corresponding to $^4A_2 \rightarrow {}^4T_2$, $^4A_2 \rightarrow {}^2T_2$ and $^4A_2 \rightarrow {}^4T_1$ transition, respectively. Though according to the spin selection rule of $\Delta S = 0$, the transitions between $^4T_2$, $^4T_1$ and ground $^4A_2$ levels are spin-allowed, the spin-forbidden transition $^4A_2 \rightarrow {}^2T_2$ is still be found in our result and other Mn-incorporated phosphors, such as CaAl$_{12}$O$_{19}$:Mn^{4+},[17] SrMgAl$_{10}$O$_{17}$:Mn^{4+},[18] Mg$_2$TiO$_4$:Mn^{4+},[10] Li$_2$Mg$_3$SnO$_6$:Mn^{4+},[19] Ba$_2$TiGe$_2$O$_8$:Mn^{4+}[20] and Na$_2$MgAl$_{10}$O$_{17}$:Mn^{4+}.[21] By fitting the peaks of the excitation spectra, we found that all the excitation peaks have a red shift as the sodium incorporated.

Crystal filed strength calculation

The values of D_q, B and C can be calculated based on experimentally determined energy levels using the following equations:[5]

Table 2 Comparison of dopant content in $Sr_4Al_{14}O_{25}:xB^{3+}, yNa^+, zMn^{4+}$

Range of x	Optimum value of x	Range of y	Optimum value of y	Optimum value of z	Excitation bands	Ref.
0.4	—	0.05	0–0.09	0.01	Synchronous increase	11
0.8	0–1.6	2	0–3	0.014	Asynchronous increase	This work

$$D_q = E(^4T_{2g} - {^4A_{2g}})/10 \tag{1}$$

$$\frac{D_q}{B} = \frac{15(x-8)}{(x^2 - 10x)} \tag{2}$$

where D_q represents the crystal field strength and the parameter x is defined as

$$x = \frac{E\left(^4A_{2g} \rightarrow {^4T_{1g}}\right) - E\left(^4A_{2g} \rightarrow {^4T_{2g}}\right)}{D_q} \tag{3}$$

$$E(^2E_g - {^4A_{2g}})/B = 3C/B + 9 - 9B/D_q \tag{4}$$

From Fig. 8a, the energy levels of $^4T_2$, $^4T_1$ and ^2E_g in the $Sr_4Al_{14}O_{25}:0.014Mn^{4+}$, $0.8B^{3+}$, $2Na^+$ host were determined at 22 124, 28 986 and 15 314 cm^{-1}, respectively. From Fig. 8b, the energy levels of $^4T_2$, $^4T_1$ and ^2E_g in the $Sr_4Al_{14}O_{25}:0.014Mn^{4+}$, $0.8B^{3+}$ host were determined at 22 321, 30 769 and 26 667 cm^{-1}, respectively. From eqn (1)–(4), the crystal field parameters of D_q, B, C in the $Sr_4Al_{14}O_{25}:0.014Mn^{4+}$, $0.8B^{3+}$, $2Na^+$ were calculated to be 2212, 644 and 3735 cm^{-1}, respectively. The crystal field parameters of D_q, B, C in the $Sr_4Al_{14}O_{25}:0.014Mn^{4+}$, $0.8B^{3+}$ were calculated to be 2232, 830 and 3540 cm^{-1}, respectively. Once these parameters have been determined, the energies of all

other states such as $^2T_1$, $^2A_1$ and $^4T_1$ can be theoretically predicted by:

$$E(^2T_1 - {^2E_g}) = 66B^2/(10D_q) \tag{5}$$

$$E(^2A_1 - {^4A_2}) = 10D_q + 4B + 3C \tag{6}$$

$$E(^4T_1(P) - {^4A_2}) = 15D_q + 7.5B \\ - 0.5[100D_q^2 - 180D_qB + 225B^2]^{1/2} \tag{7}$$

The crystal field parameters and the energies of states in $Sr_4Al_{14}O_{25}:0.014Mn^{4+}$, $0.8B^{3+}$, $2Na^+$ and $Sr_4Al_{14}O_{25}:0.014Mn^{4+}$, $0.8B^{3+}$ crystal lattices are summarized in the Table 3. As shown in Fig. 8c, the dependence of energy levels of Mn^{4+} on crystal field strength can be illustrated by Tanabe–Sugano energy diagram. The ^2E_g levels are almost parallel to the ground state $^4A_2$, which results that the location of the emission peak is difficult to be influenced by crystal field strength. While, the energy gap between $^4T_1$ (or $^4T_2$) levels and ground state $^4A_2$ can be changed by variation of the crystal field strength. The electron transition schematic diagrams are shown in the Fig. 8c with blue and green dot lines. The value of D_q/B increased to 3.43 from 2.69 as the Na^+ ions addition. There is a difference in the asynchronous increases of the near UV and visible absorption bands. The increase of the excitation
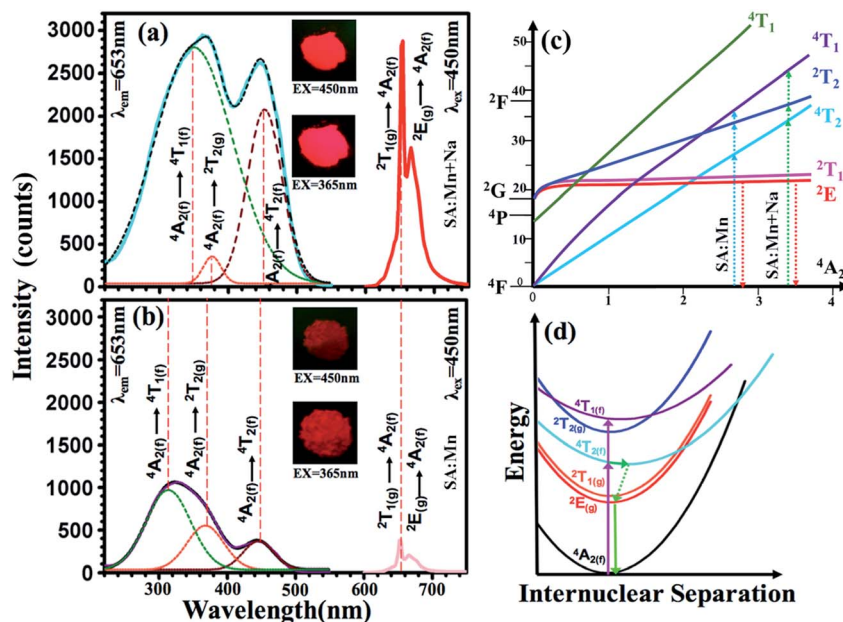

Fig. 8 (a) PL (EX = 450 nm) and PLE (EM = 652 nm) spectra of $Sr_4Al_{14}O_{25}:0.014Mn^{4+}$, $2Na^+$, $0.8B^{3+}$ and (b) $Sr_4Al_{14}O_{25}:0.014Mn^{4+}$, $0.8B^{3+}$ respectively; (c) Tanabe–Sugano energy diagram of a $3d^3$ system in an octahedral crystal field; (d) configurational coordinate diagram for Mn^{4+} ions in $Sr_4Al_{14}O_{25}$ hosts.

Table 3 Crystal field parameters and energies of states in $Sr_4Al_{14}O_{25}$:$0.014Mn^{4+}$, $0.8B^{3+}$, $2Na^+$ and $Sr_4Al_{14}O_{25}$:$0.014Mn^{4+}$, $0.8B^{3+}$ crystal lattices

	$Sr_4Al_{14}O_{25}$:$0.014Mn^{4+}$, $0.8B^{3+}$, $2Na^+$ (cm^{-1})	$Sr_4Al_{14}O_{25}$:$0.014Mn^{4+}$, $0.8B^{3+}$ (cm^{-1})
D_q	2212	2232
B	644	830
C	3735	3540
D_q/B	3.43	2.69
$^4A_2 \rightarrow {^4T_2}$	22 124	22 321
$^4A_2 \rightarrow {^2T_2}$	26 455	26 667
$^4A_2 \rightarrow {^4T_1}$	28 985	30 769
$^2E_g \rightarrow {^4A_2}$	15 314	15 314
$^2E_g \rightarrow {^2T_1}$	1238	2039
$^4A_2 \rightarrow {^2A_1}$	35 905	36 264
$^4A_2 \rightarrow {^4T_1}$	28 986	30 769

intensity at visible blue region is much larger than at near UV region, even both excitation intensity at these two regions are almost equal. Na^+ compounds are well known fluxes in solid state synthesis. However, the shapes of the excitation bands cannot be changed by fluxes and meanwhile the redshift of the excitation is a change on the luminous mechanism instead of fluxes effect.

Fig. 8d shows a schematic diagram of a process of photo-luminescence. The ^2E_g, $^2T_1$, $^2T_2$ and $^4A_2$ levels are derived from the t_2^3 electronic orbital, whereas the $^4T_1$ and $^4T_2$ levels are formed from another t_2^2e orbital, resulting a displacement between the parabolas of ground state $^4A_2$ and $^4T_1$ (or $^4T_2$). The electronics are excited from to ground state $^4A_2$ to $^4T_1$, $^4T_2$ or $^2T_2$ levels by radiation. Then, the excited electronics usually relax non-radiatively to ^2E_g followed by the spin-forbidden $^2E_g \rightarrow {^4A_2}$ transition characterized by wide emission bands.

Conclusions

A series of $Sr_4Al_{14}O_{25}$:xB^{3+}, yNa^+, zMn^{4+} red phosphors were synthesized by a high-temperature solid-state reaction method at 1400 °C for 6 hours in the air. The fluorescent intensities of the phosphors excited at 450 nm reached a maximum at $x = 0.8$, $y = 2$ and $z = 0.014$, and the strongest emission intensity of $Sr_4Al_{14}O_{25}$:$0.8B^{3+}$, $2Na^+$, $0.014Mn^{4+}$ sample were increased by 700% compared with $Sr_4Al_{14}O_{25}$:$0.8B^{3+}$, $0.014Mn^{4+}$ without Na^+ co-doping. In comparison with Mn^{4+} single incorporated phosphor, $Sr_4Al_{14}O_{25}$:$0.014Mn^{4+}$, $0.8B^{3+}$, $2Na^+$ shows greater advantage of promising application incorporated as a red component into blue chip-based LED for plant growth because of much stronger absorption at blue light region and enhanced red emission. The prepared phosphors could be efficiently excited by both near-UV light and the commercially available blue light of LED chips at 450 nm.

Conflicts of interest

There are no conflicts to declare.

Acknowledgements

References

1 K. Okamoto, T. Yanagi, S. Takita, M. Tanaka, T. Higuchi, Y. Ushida and H. Watanabe, Development of plant growth apparatus using blue and red LED as artificial light source, *Acta Hortic.*, 1996, **440**, 111.

2 E. C. Wassink and J. A. J. Stol Wijk, Effects of Light Quality on Plant Growth, *Annu. Rev. Plant Physiol.*, 1956, **7**, 373–400.

3 K. Okamoto and T. Yanagi, *Development of light source for plant growth using blue and red super-bright LEDs*, Shikoku-Section Joint Convention Record of the Institute of Electrical and Related Engineers, 1994, p. 109.

4 R.-J. Xie, N. Hirosaki, T. Suehiro, F.-F. Xu and M. Mitomo, A Simple, Efficient Synthetic Route to $Sr_2Si_5N_8$:Eu^{2+}-Based Red Phosphors for White Light-Emitting Diodes, *Chem. Mater.*, 2006, **18**, 5578–5583.

5 H. Zhu, C. Che Lin, W. Luo, S. Shu, Z. Liu, Y. Liu, J. Kong, E. Ma, Y. Cao, R.-S. Liu and X. Chen, Highly efficient non-rare-earth red emitting phosphor for warm white light-emitting diodes, *Nat. Commun.*, 2014, **5**, 4312.

6 D. Chen, Y. Zhou and J. Zhong, A review on Mn^{4+} activators in solids for warm white light-emitting diodes, *RSC Adv.*, 2016, **6**, 86285–86296.

7 C. L. Comar and F. P. Zscheile, Analysis Of Plant Extracts For Chlorophylls A And B By A Photoelectric Spectrophotometric Method, *Plant Physiol.*, 1942, **17**, 198–209.

8 D. Chen, Y. Zhou, W. Xu, J. Zhong, Z. Ji and W. Xiang, Enhanced Luminescence of Mn^{4+}:$Y_3Al_5O_{12}$ via Impurity Doping, *J. Mater. Chem. C*, 2016, **4**, 1704–1712.

9 M. Peng, X. Yin, P. A. Tanner, M. G. Brik and P. Li, Site Occupancy Preference, Enhancement Mechanism, and Thermal Resistance of Mn^{4+} Red Luminescence in $Sr_4Al_{14}O_{25}$:Mn^{4+} for Warm WLEDs, *Chem. Mater.*, 2015, **27**, 2938–2945.

10 Z. Qiu, T. Luo, J. Zhang, W. Zhou, L. Yu and S. Lian, Effectively enhancing blue excitation of red phosphor Mg_2TiO_4:Mn^{4+} by Bi^{3+} sensitization, *J. Lumin.*, 2015, **158**, 130–135.

11 L. Wang, Y. Xu, D. Wang, R. Zhou, N. Ding and M. Shi, Deep red phosphors $SrAl_{12}O_{19}$:Mn^{4+}, M (M = Li^+, Na^+, K^+, Mg^{2+}) for high colour rendering white LEDs, *Phys. Status Solidi*, 2013, **210**(7), 1433–1437.

12 L. Meng, L. Liang and Y. Wen, A novel red phosphor Na^+, Mn^{4+} co-doped $Sr_4Al_{14}O_{25}$ for warm white light emitting diodes, *Mater. Chem. Phys.*, 2015, **153**, 0254–0584.

13 K. Momma and F. Izumi, VESTA 3 for three-dimensional visualization of crystal, volumetric and morphology data, *J. Appl. Crystallogr.*, 2011, **44**, 1272.

14 Y. D. Xu, D. Wang, L. Wang, N. Ding, M. Shi and J. G. Zhong, Preparation and luminescent properties of a new red

phosphor ($Sr_4Al_{14}O_{25}$:Mn^{4+}) for white leds, *J. Alloys Compd.*, 2013, **550**, 226–230.

15 M. Peng, X. Yin, P. A. Tanner, C. Liang, P. Li and Q. Zhang, Orderly-layered tetravalent manganese-doped strontium aluminate $Sr_4Al_{14}O_{25}$:Mn^{4+}: an efficient red phosphor for warm white light emitting diodes, *J. Am. Ceram. Soc.*, 2013, **96**, 2870–2876.

16 M. G. Brik, S. J. Camardello and A. M. Srivastava, Influence of covalency on the Mn^{4+} $^2E_g \rightarrow$ $^4A_{2g}$ emission energy in crystals, *ECS J. Solid State Sci. Technol.*, 2015, **4**, R39–R43.

17 T. Murata, T. Tanoue, M. Iwasaki, K. Morinaga and T. Hase, Fluorescence properties of Mn^{4+}, in $CaAl_{12}O_{19}$ compounds as red-emitting phosphor for white LED, *J. Lumin.*, 2005, **114**, 207–212.

18 L. Meng, L. Liang and Y. Wen, Deep red phosphors $SrMgAl_{10}O_{17}$:Mn^{4+}, M (M = Li^+, Na^+, K^+, Cl^-) for warm white light emitting diodes, *J. Mater. Sci.: Mater. Electron.*, 2014, **25**, 2676–2681.

19 R. Cao, J. Zhang, W. Wang, Z. Hu, T. Chen, Y. Ye and X. Yu, Preparation and photoluminescence characteristics of $Li_2Mg_3SnO_6$:Mn^{4+}, deep red phosphor, *Mater. Res. Bull.*, 2017, **87**, 109–113.

20 R. Cao, Y. Ye, Q. Peng, G. Zheng, H. Ao, J. Fu, Y. Guo and B. Guo, Synthesis and luminescence characteristics of novel red-emitting $Ba_2TiGe_2O_8$:Mn^{4+} phosphor, *Dyes Pigm.*, 2017, **146**, 14–19.

21 Q. Peng, R. Cao, Y. Ye, S. Guo, Z. Hu, T. Chen and G. Zheng, Photoluminescence properties of broadband deep-red-emitting $Na_2MgAl_{10}O_{17}$:Mn^{4+} phosphor, *J. Alloys Compd.*, 2017, **725**, 139–144.